

Discontinuous Galerkin scheme for turbulent flow simulations

By P. C. Ma, Y. Lv AND M. Ihme

1. Motivation and objectives

Recent progress in applying the discontinuous Galerkin (DG) schemes for direct numerical simulation (DNS) and large eddy simulation (LES) of turbulent flows is attributed to the improvement in the stability and robustness of conventional methods. In particular, significant advances have been made with regard to the development of DG discretization for elliptic equations, including schemes of symmetric interior penalty (Arnold *et al.* 2002), BR1 (Bassi & Rebay 1997), BR2 (Bassi & Rebay 2000), local DG method (Cockburn & Shu 1998) and compact DG method (Peraire & Persson 2008). Another algorithmic contribution to enable DG for turbulence flow is its improved robustness. More suitable stabilization techniques of the DG scheme for turbulence simulation are probably the positivity-preserving (Zhang & Shu 2010, 2011) and the entropy-bounded (Lv & Ihme 2015) DG schemes, each ensuring generality and practical simplicity. Both methods have rigorous mathematical foundation to guarantee the scheme's robustness.

Given the considerable progress made towards diffusion discretization and algorithmic robustness, the DG scheme currently is better established for high-fidelity simulations of turbulence. The question that arises naturally is whether the high-order variational scheme has advantages over classical finite difference (FD) and finite volume (FV) schemes. Carton de Wiart *et al.* (2014) compared the performance of the DG scheme to a non-dissipative FD scheme in predicting inviscid vortical flow. It was found that the benefit of the non-dissipative property of the FD scheme was offset by the dispersive error apparent for medium wavenumbers of the energy spectrum. In the context of LES, Gassner & Beck (2013) attempted to assess the performance of DG for highly underresolved turbulent flows. They found that simulations without explicitly adding sub-grid scale (SGS) terms are comparable to results generated by low-order schemes with SGS models. In order to support model development, greater insight into the aspect of numerics of the DG discretization and behavior compared to classical non-dissipative FD and FV methods is required.

The remainder of this report has the following structure. Section 2 introduces the DG discretization for Navier-Stokes equations. Algorithmic details about the FV solver, CharlesX, are introduced in Section 2. After test cases are described in Section 3, the accuracy in predicting characteristic turbulent quantities are compared and the effects of refinement strategy on solutions are discussed in Section 4. The report finishes with conclusions in Section 5.

2. Mathematical formulations

2.1. Governing equations

The governing equations are the conservations of mass, momentum and total energy as follows

$$\partial_t \rho + \nabla \cdot (\rho \mathbf{u}) = 0, \quad (2.1a)$$

$$\partial_t (\rho \mathbf{u}) + \nabla \cdot (\rho \mathbf{u} \mathbf{u} + p \mathbf{I}) = \nabla \cdot \boldsymbol{\tau}, \quad (2.1b)$$

$$\partial_t (\rho e) + \nabla \cdot (\rho \mathbf{u} (e + p/\rho)) = -\nabla \cdot \mathbf{q} + \nabla \cdot (\boldsymbol{\tau} \cdot \mathbf{u}), \quad (2.1c)$$

where the viscous stress tensor and conductive heat flux are written as

$$\boldsymbol{\tau} = \mu \left[\nabla \mathbf{u} + (\nabla \mathbf{u})^T \right] - \frac{2}{3} \mu (\nabla \cdot \mathbf{u}) \mathbf{I}, \quad (2.2a)$$

$$\mathbf{q} = -\lambda \nabla T. \quad (2.2b)$$

This system of equations is closed with the ideal gas relation

$$p = (\gamma - 1) \left(\rho e - \frac{1}{2} \rho |\mathbf{u}|^2 \right), \quad (2.3)$$

where γ is the heat-capacity ratio. For notational convenience, in the following the scheme formulation is written in the vector form as

$$\partial_t \mathbf{U} + \nabla \cdot \mathbf{F} = \nabla \cdot \mathbf{Q}, \quad (2.4)$$

in which \mathbf{U} , \mathbf{F} and \mathbf{Q} refer to the solution vector, the convection flux and the viscous flux, respectively.

2.2. DG discretization

To discretize Eq. (2.4) with a variational approach, a broken space is used as the test space

$$\mathcal{V}_h^p = \{ \phi \in L^2(\Omega) : \phi_e \equiv \phi|_{\Omega_e} \in \mathcal{P}_p, \forall \Omega_e \in \Omega \}, \quad (2.5)$$

in which a polynomial space with order p is defined on each individual element Ω_e resulting from the domain partition. The test function ϕ is then multiplied to Eq. (2.4) to derive the weak form. The left-hand-side of Eq. (2.4) is the classical Euler equations, and the corresponding weak and Galerkin forms can be obtained

$$\begin{aligned} \int_{\Omega} \phi (\partial_t \mathbf{U} + \nabla \cdot \mathbf{F}) dx &= \sum_e \left(\int_{\Omega_e} (\phi_e \partial_t \mathbf{U} - \nabla \phi_e \cdot \mathbf{F}) dx + \int_{\partial \Omega_e} \phi_e^+ \mathbf{F} \cdot \mathbf{n} ds \right) \\ &\approx \sum_e \left(\int_{\Omega_e} \phi_e \phi_e^T d_i \tilde{U}_{e,i}(t) dx - \int_{\Omega_e} \nabla \phi_e \cdot \mathbf{F}(U_e) dx + \int_{\partial \Omega_e} \phi_e^+ \hat{F} ds \right), \end{aligned} \quad (2.6)$$

in which the superscript “+” refers to interior quantity on element edge and the discretized solution U (together with U_e and $\tilde{U}_{e,i}$), following the Galerkin method, takes the form

$$\mathbf{U} \simeq U = \bigoplus_{e=1}^{N_e} U_e, \quad (2.7a)$$

$$U_e(t, x) = \sum_{i=1}^{N_p} \tilde{U}_{e,i}(t) \phi_{e,i}(x). \quad (2.7b)$$

To complete the discretization, the Riemann flux \hat{F} in Eq. (2.6) needs to be specified, for which we consider the preconditioned Roe scheme (Turkel *et al.* 1997) for the current study.

Since \mathbf{Q} involves multi-entries, here we only consider a general form for each of them to simplify the explanation. \mathbf{Q}_i denotes the diffusion flux of Navier-Stokes equations for the i^{th} solution variable. This can be further represented using a linearization $\mathbf{Q}_i = \sum_j \mathbf{D}_{ij} \circ \nabla \mathbf{U}_j$, where \circ refers to Hadamard product. Because the discretization is subject to the distributive property of addition, the problem can be further simplified by discretizing $\mathbf{D}_{ij} \circ \nabla \mathbf{U}_j \equiv \mathbf{Q}_{ij}$ taking the following form

$$\begin{aligned} \sum_e \int_{\Omega_e} \phi \nabla \cdot \mathbf{Q}_{ij} dx &= \sum_e \left(- \int_{\Omega_e} (\mathbf{D}_{ij} \circ \nabla \mathbf{U}_j) \cdot \nabla \phi_e dx + \int_{\partial \Omega_e} \phi_e \mathbf{Q}_{ij} \cdot \mathbf{n} ds \right) \\ &= \sum_e \left(\int_{\Omega_e} \mathbf{U}_j \nabla \cdot (\mathbf{D}_{ij} \circ \nabla \phi_e) dx - \int_{\partial \Omega_e} \mathbf{U}_j (\mathbf{D}_{ij} \circ \nabla \phi_e) \cdot \mathbf{n} ds + \int_{\partial \Omega_e} \phi_e \mathbf{Q}_{ij} \cdot \mathbf{n} ds \right) \\ &\approx \sum_e \left(\int_{\Omega_e} \mathbf{U}_j \nabla \cdot (\mathbf{D}_{ij} \circ \nabla \phi_e) dx - \int_{\partial \Omega_e} \widehat{\mathbf{U}}_j (\mathbf{D}_{ij} \circ \nabla \phi_e)^+ \cdot \mathbf{n} ds + \int_{\partial \Omega_e} \phi_e^+ \widehat{\mathbf{Q}}_{ij} ds \right) \\ &= \sum_e \left(- \int_{\Omega_e} \nabla \phi_e \cdot (\mathbf{D}_{ij} \circ \nabla \mathbf{U}_j) dx + \int_{\partial \Omega_e} (\mathbf{U}_j^+ - \widehat{\mathbf{U}}_j) (\mathbf{D}_{ij} \circ \nabla \phi_e)^+ \cdot \mathbf{n} ds + \int_{\partial \Omega_e} \phi_e^+ \widehat{\mathbf{Q}}_{ij} ds \right). \end{aligned}$$

With this, the discretization of $\nabla \cdot \mathbf{Q}_i$ can be written as

$$\begin{aligned} \sum_e \int_{\Omega_e} \phi \nabla \cdot \mathbf{Q}_i dx &\approx \\ \sum_e \left(- \int_{\Omega_e} \nabla \phi_e \cdot ([D_i]^T \nabla U) dx + \int_{\partial \Omega_e} ([D_i^+]^T (U^+ - \widehat{U}) \circ \nabla \phi_e) \cdot \mathbf{n} ds + \int_{\partial \Omega_e} \phi_e^+ \widehat{Q}_i ds \right), \end{aligned} \quad (2.8)$$

where the diffusion Jacobian $[D_i]$ has number N_s of rows composed of D_{ij} . The three terms on the right-hand side account for interior diffusion, dual consistency and inter-element diffusion. \widehat{U} and \widehat{Q} can be selected in various ways, which distinguish different diffusion-discretization schemes. In this study, we consider the standard interior penalty (SIP) method (Arnold *et al.* 2002) and \widehat{U} is chosen to be $\{U\}^\dagger$, then we have

$$\widehat{Q}_i = \{[D_i]^T \nabla U\} + \sigma_{\text{SIP}} \left(\max_{x \in \partial \Omega_e^\pm} \mu(x) \right) \llbracket U \rrbracket / h, \quad (2.9)$$

where σ refers to constant parameters to ensure numerical stability. As for σ_{SIP} , we use the suggested values in Shahbazi (2005). The stabilization term for \widehat{Q}_i in Eq. (2.9), which has a consistent form of that in the Riemann solvers, always behaves as a dissipation term, but the entire term, \widehat{Q}_i , is not guaranteed to be always dissipative.

2.3. Finite volume solver CharlesX

To facilitate a comparison of DG scheme with a FV discretization, we consider CharlesX. This solver has been developed by researchers at Center for Turbulence Research, Stanford University. CharlesX has been applied to studies of aeroacoustics (Nichols *et al.* 2012), supercritical flow (Hickey *et al.* 2013), supersonic combustion (Larsson *et al.* 2015), and aerodynamic flows (Bodart *et al.* 2013), etc. The governing equations for mass, momentum, and total energy are solved along with the ideal gas law (Eqs. (2.1)-(2.3)). Here a brief summary of the numerics is presented, and for more details we refer the reader to the work by Ham & Iaccarino (2004) and Khalighi *et al.* (2011). CharlesX was developed based on a reconstruction-based FV scheme. Polynomials with maximum third-order accuracy are used to reconstruct the left- and right-biased face centroid values of the flow variables, and a blending between the central and Riemann flux is computed based on the

$$\dagger \{ \cdot \} = ((\cdot)^+ + (\cdot)^-)/2, \quad \llbracket \cdot \rrbracket = (\cdot)^+ n^+ + (\cdot)^- n^-$$

Case No.	Re_λ	M_t	ν	p	η
1	40	0.1	1.25×10^3	214.3	0.04
2	40	0.6	1.25×10^3	5.95	0.04
3	100	0.6	5.0×10^3	5.95	0.026
4	100	1.5	5.0×10^3	0.95	0.026

Table 1. Operating conditions for the HIT cases; initial values at $t = 0$ are listed.

local grid quality. This flux computation procedure yields formally second-order accuracy and has maximum fourth-order accuracy on perfectly uniform Cartesian mesh, without numerical dissipation. For computations of shock-related problems, CharlesX utilizes a sensor-based hybrid Central-ENO scheme to minimize the numerical dissipation while stabilizing the simulation. For regions where shocks are present, a second-order ENO reconstruction is used on the left- and right-biased face values, followed by an HLLC Riemann flux computation. A number of different hybrid sensors/switches are available within CharlesX. For the current study, the relative solution (RS) sensor is adopted. This sensor compares the difference between the left- and right-biased polynomial reconstructed face values of density and pressure to the minimum of the corresponding values in the two neighboring cells of the face. When the difference exceeds a certain fraction of the minimum cell value, the ENO reconstruction scheme will be used. For the following study, a value of 0.5 was found to be sufficiently effective. The semi-discretized form is solved using a fully explicit, fourth-order Runge-Kutta time integration scheme.

3. Problem setup and flow configurations

In order to mimic realistic turbulence, we consider the decaying homogeneous isotropic turbulence (HIT) for comparative study. Four different cases are considered covering a range of representative operating conditions. As listed in Table 1, these cases are characterized by the initial turbulent Reynolds number, $\text{Re}_\lambda = \langle \rho \rangle \lambda \sqrt{\langle u^2/3 \rangle} / \langle \mu \rangle$, and the initial turbulent Mach number, $M_t = \sqrt{\langle u^2 \rangle} / \langle c \rangle$, where $u = \sqrt{u_1^2 + u_2^2 + u_3^2}$, c is the speed of sound, and λ is the Taylor microscale. Conservation equations are solved in a 3D periodical domain of $[-\pi, \pi] \times [-\pi, \pi] \times [-\pi, \pi]$. The specific heat ratio, γ , is set to a value of 1.4. The molecular viscosity is calculated by considering the power-law dependence on temperature, $\mu/\mu_{\text{ref}} = (T/T_{\text{ref}})^{0.76}$. Initial conditions for the current study are given by a divergence-free velocity field and constant thermodynamic quantities. The energy spectrum for the initial field for u is prescribed to be

$$E_u(k) \sim k^4 \exp(-2k^2/k_0^2), \quad (3.1)$$

where k_0 is the most energetic wavenumber, related to the Taylor microscale λ . In Table 1, a combination of different Re_λ and M_t is presented along with the corresponding thermodynamic quantities and Kolmogorov length scale η . In the following, results are presented with time normalized by the eddy turnover time $\tau = \lambda / \sqrt{\langle u^2/3 \rangle}$.

Two different mesh configurations are considered for this study, as illustrated in Figure 1, consisting of regular hexahedral and tetrahedral elements. The tetrahedral mesh is generated by cutting one hexahedron into five tetrahedra. To represent the elemental geometry in the DG solver, linear Lagrangian nodal bases are employed.

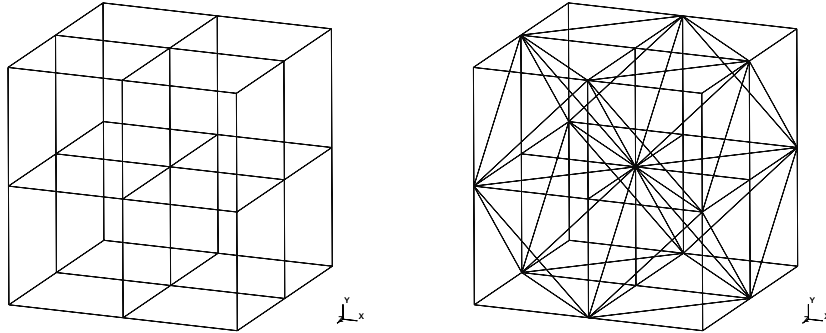


Figure 1. Illustration of the mesh settings in $2 \times 2 \times 2$ setting.

4. Results and discussions

4.1. Comparison of converged solution

This section compares the solutions obtained from DG and FV solvers on the finest mesh in order to examine the consistency of the resolved solutions. For this part of the study, the regular hexahedral mesh is employed, for which the FV solver provides a fourth-order non-dissipative discretization. To retain a consistent discretization, a fourth-order DG scheme, DGP3, is used as the counterpart. Based on the estimation of the Kolmogorov scale, it is found that cases with $Re = 40$ are sufficiently resolved using 128 cells in each direction with CharlesX, whereas cases with $Re = 100$ are well-resolved using 256^3 cells. For the case with $M_t = 1.5$, the resolution requirement is more restrictive due to the presence of strong dilatation effects. Because of the strong dilatation, the shock-capturing capability of CharlesX is activated. About one percent of the overall cells are detected by the built-in shock sensor and treated with the ENO discretization when 256^3 cells are used. The convergence for all the characteristic quantities is achieved and verified through a mesh-refinement study. Under the resolved mesh resolution, excellent agreement on the predicted characteristic quantities is presented and observed in Figure 2. Since the predictions are obtained from two completely different methods and implementations, this agreement on different aspects further underpins the credibility of the solution predicted by both methods. The only noticeable difference is in the deviation of the energy close to the cutoff wavenumber. The FV scheme obtains a coherent energy cascade, consistent with turbulence physics. The pile-up of energy for the DG-scheme might be due to the aliasing error accumulated in the DG solutions, or have been generated during signal sampling onto the FFT grid. The same issue was also found by Carton de Wiart *et al.* (2014). Given this small difference in the energy spectrum, the predictive capability of the FV- and DG-schemes can be considered identical.

4.2. Comparison of under-resolved solutions

In this section, we focus on under-resolved solutions. The accuracy of different schemes is assessed by observing the convergence speed with respect to the resolved reference data. Furthermore, examining the solution behavior on a under-resolved mesh will provide useful insight on how to develop LES modeling strategies taking into account the specific scheme characteristics. We focus directly on the comparison of predicted velocity spectra,

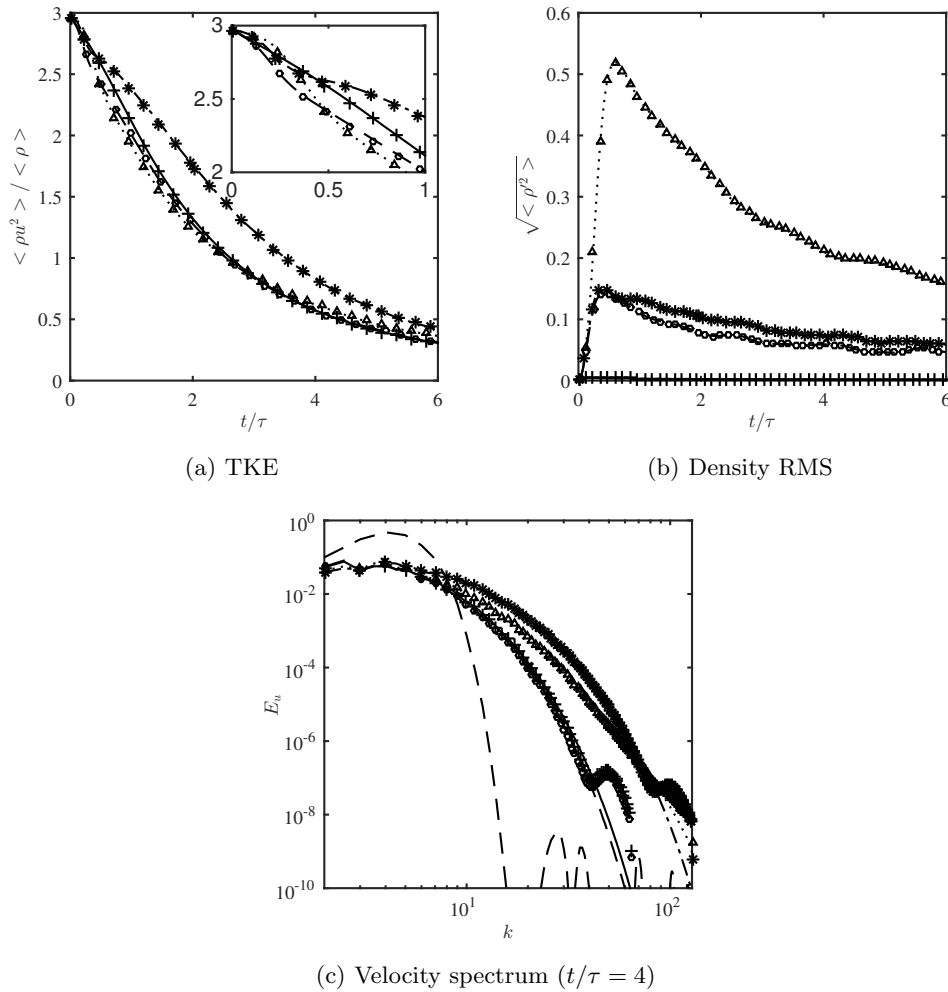


Figure 2. Resolved solutions obtained by both DG and FV solvers (solid line and + symbol— $\text{Re} = 40$, $\text{Mt} = 0.1$; dashed line and \circ symbol— $\text{Re} = 40$, $\text{Mt} = 0.6$; dash-dot line and * symbol— $\text{Re} = 100$, $\text{Mt} = 0.6$; dotted line and \triangle symbol— $\text{Re} = 100$, $\text{Mt} = 1.5$; lines—FV results; symbols—DG solutions; the initial interpolated spectrum on DG space is also shown as dashed line in the last figure).

which are presented in Figure 3. A fundamental difference in the predicted spectra can be observed near the region around the cutoff wavenumber. Significant energy overshoots are generated by the non-dissipative FV scheme for under-resolved DNS. This was recognized as a common issue of the scheme (Larsson *et al.* 2007) and led to the development of compatible SGS models (Moin *et al.* 1991; Kosović *et al.* 2002). Besides this issue, attention should also be drawn to the intermediate wavenumber range. As shown in Figure 3(a), the zoom-in plot emphasizes a drainage of energy induced by the central FV scheme between the wavenumbers 4 and 8. This spectral contamination at this range of wavenumber was also recognized previously in Fureby *et al.* (1997), and it is likely due to the dispersive error inherent in the non-dissipative scheme (Carton de Wiart *et al.*

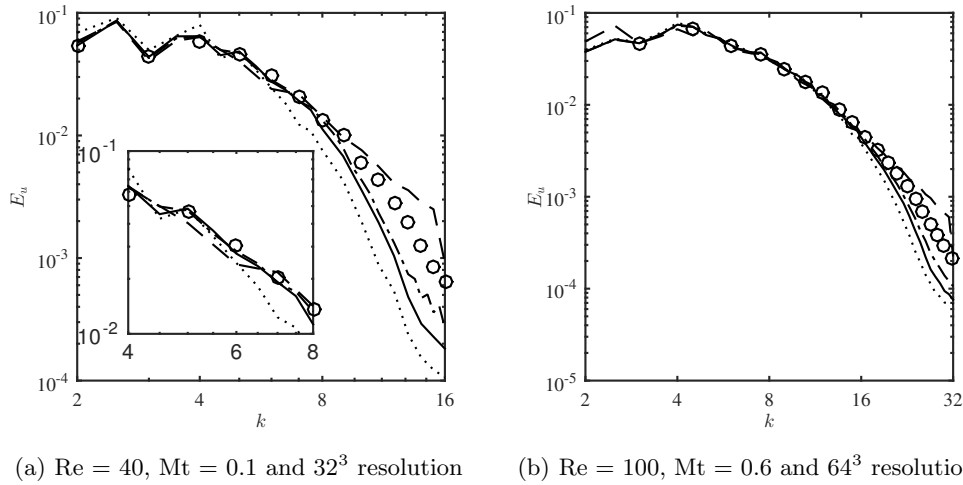


Figure 3. Velocity spectra of under-resolved solutions at $t/\tau = 4$ (\circ symbol—converged reference spectrum; dash-dot line—DGP4; solid line—DGP3; dotted line—DGP2; dashed line—FV).

2014). For the DG-scheme, the inherent numerical dissipation from both convection and diffusion flux stabilization terms leads to the energy undershoots at small scales. This observation explains the good performance of the DG-scheme applied to certain implicit LES-applications (Beck *et al.* 2014; Carton de Wiart *et al.* 2015). Note that because the DG-scheme is already dissipative at small scales, in general we cannot expect performance improvement by simply applying SGS models developed for non-dissipative schemes. Hence, the LES modeling strategy for DG might have to rely on a completely new perspective.

The compressibility introduces a significant interaction with turbulent flows. The effect of compressibility is typically characterized in forms of changes of induced thermodynamic variables. For this, the density root-mean-square (RMS) is selected to assess the performance and results are given in Figure 4. Generally speaking, DGP3 seems more effective in accurately predicting density RMS. At a low-Mach case, DGP3 and the fourth-order FV scheme perform equally well, while DGP2 leads to overshoots in the coarsest mesh. This observation implies that improvement of polynomial order is more effective in representing thermodynamic fluctuation than refining element size. This is likely because the thermodynamic variation is acoustic-controlled under this operating condition and the prediction of acoustics often requires spectral-like resolution, thereby being improved by using schemes with higher order. At an intermediate Mach-number regime, the central-based FV scheme overpredicts the density fluctuation, induced by the more energetic small scales generated by the non-dissipative numerics. For the DG scheme, the performance of DGP2 and DGP3 are comparable given the same number of degree of freedoms (DoFs). For the fourth case ($\text{M}_t = 1.5$), the CharlesX relies on a sensor-based shock-capturing strategy for scheme stabilization, since fully central formulation leads to solution divergence. Built on previous investigations and heuristics gathered from applications, the CharlesX shock-capturing become well-established for turbulent-oriented applications. This advantage is clearly illustrated in Figure 4(d). Under the same resolution, CharlesX provides more accurate predictions for density fluctuation than the DG

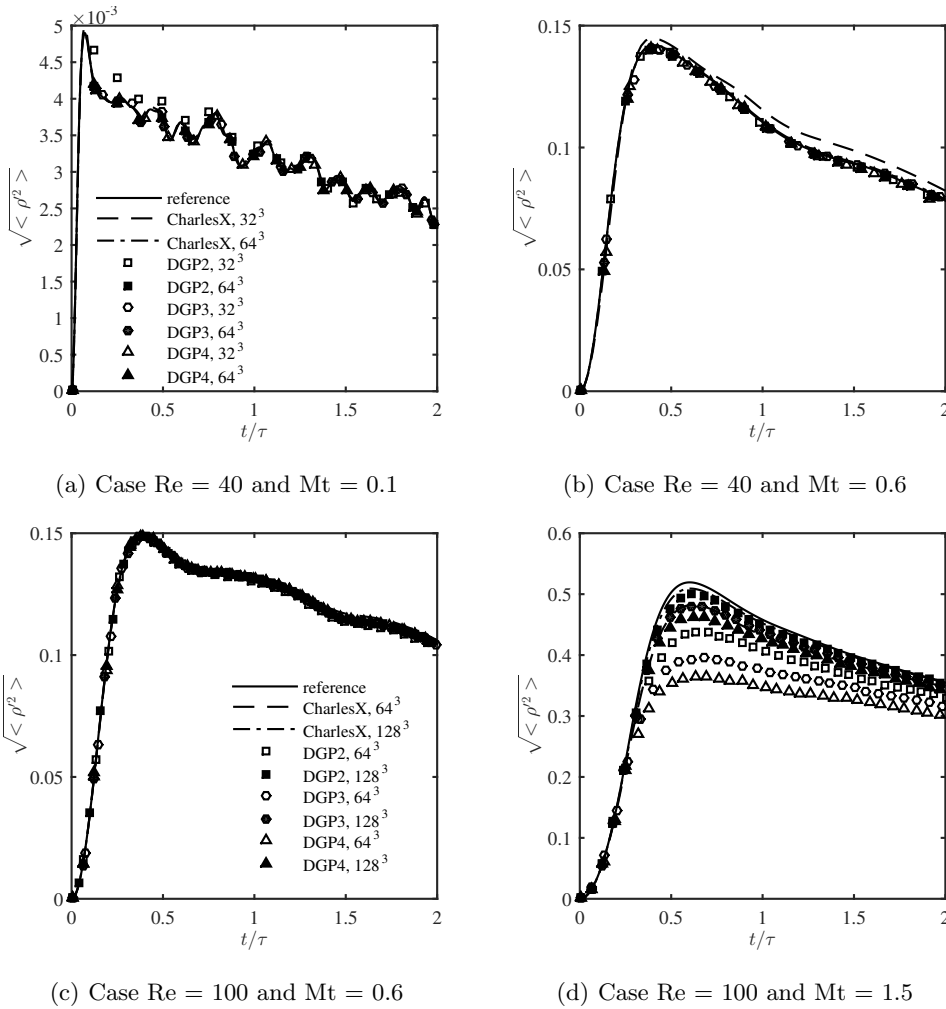


Figure 4. Density RMS of under-resolved solutions (first two figures share the legend in figure (a) and the last two share the one in figure (c)).

schemes, likely due to the strong shocklets generated in this case, a result which challenges the local polynomial approximation of DG solutions. The underprediction by DG indicates this solution approximation might overly constrain the evolution of thermodynamic quantities. In addition, it is also interesting to see that DGP2 provides better overall predictions than DGP3, suggesting that h -refinement is more effective than p -refinement for this operating condition.

In summary, for all the considered turbulence-related quantities, we do not observe pronounced advantages of DG over CharlesX on the regular mesh for the same DoF and order of accuracy. Comparing three DG schemes, namely third-order DGP2, fourth-order DGP3 and fifth-order DGP4, the latter two have apparent advantages over the former in representing turbulence-induced density fluctuation characteristics at relatively low Mach number conditions. However, for a highly compressible turbulence regime, the observation is the reverse. This issue is essentially associated with the smoothness of the solution.

Higher-order schemes are more effective in resolving smooth solutions, while finer meshes are more appropriate for capturing discontinuous solutions. This observation, although contradictory, in fact agrees well with current understanding of high-order schemes (Wang *et al.* 2013).

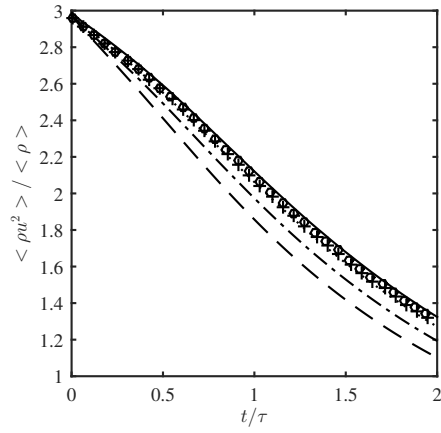
4.3. Comparison of solutions on tetrahedron meshes

For the FV scheme CharlesX, a blending of central and Riemann flux based on the local grid quality is required for stabilization (Khalighi *et al.* 2011). A heuristic blending parameter based on the skew-symmetric property of the differencing operator is employed. The blending parameter is purely grid based and can be evaluated prior to the simulation. For uniform Cartesian grids in previous subsections, the pre-computed blending parameter yields a purely central flux for all computational faces since the differencing operations in CharlesX using polynomial interpolation give a skew-symmetric operator. However, for the tetrahedron meshes considered in this part of study, a bias of Riemann flux is needed to ensure the scheme's stability. A number of 7.5% of the computational faces is found to be sufficiently efficient for this purpose. On these faces, the HLLC Riemann solver is applied.

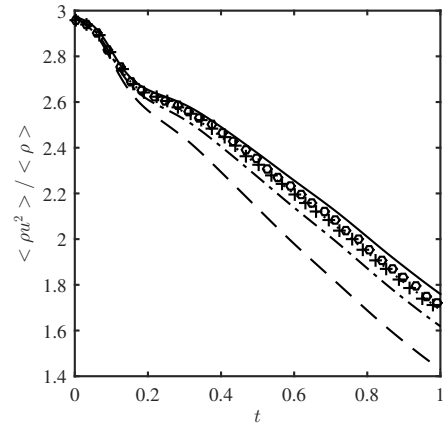
For comparison, resolutions used for the DG scheme are 5×16^3 for DGP3 and 5×22^3 for DGP2, which yield a nearly identical resolution of 5×44^3 for the FV scheme. On this type of mesh, apart from the effect of flux blending on accuracy, the convergence of CharlesX also deteriorates to second order. The degradation of accuracy significantly impairs the predictions of all turbulence quantities. As shown in Figure 5, under the same resolution (5×44^3), the FV results are significantly poorer than those for the DG-schemes. Further mesh refinement is conducted for the FV scheme, from which we can see that the FV provides a comparable prediction for turbulent kinetic energy (TKE) and spectrum with another two levels of mesh refinement; however, the prediction of density RMS is still far off the DG predictions for the case with $Re_\lambda = 40$ and $M_t = 0.1$, given the strong sensitivity of density fluctuation to numerical error. The slow convergence also reminds us of the difficulty of discretizing the viscous terms with FV scheme on unstructured mesh (Diskin *et al.* 2010). In CharlesX, the viscous terms are not treated in a completely weak sense, for which the derivatives, for example representing viscous stress and heat conduction, still rely on the approximation of strong formulation. This treatment limits the accuracy of FV schemes on irregular meshes. However, the diffusion discretization for the DG scheme, which is built completely on a weak formulation, provides more attractive advantages for the scheme.

5. Conclusions

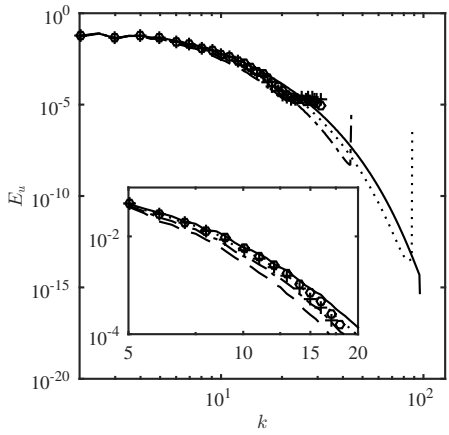
The DG scheme is compared to a state-of-art FV solver, CharlesX, developed at the Center of Turbulence Research, Stanford University. The turbulence case considered in this study is the isotropic decaying turbulence for which the characteristic quantities, including TKE, velocity spectrum, and density fluctuation, are predicted and compared. It is found that on regular hexahedral mesh, the accuracy of DGP3 and the fourth-order FV scheme is comparable, except for the fundamental difference in the under-resolved velocity spectrum. Energy pile-up at small scales is found in the under-resolved velocity spectrum of the non-dissipative FV scheme, while the DG scheme (P2 to P4) leads to energy under-shoots at the same range of wavenumbers. This is attributed to the numerical dissipation inherent in the scheme. This finding implies that the subgrid modeling strategy for the DG scheme might require a new perspective.



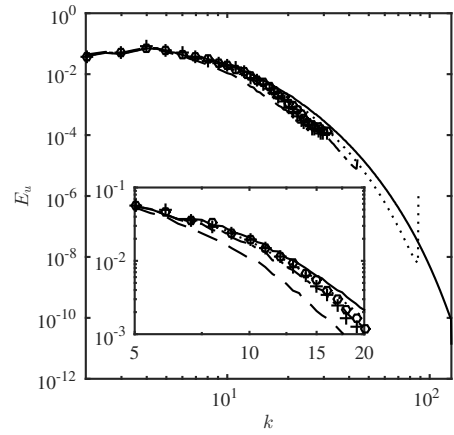
(a) TKE for $Re = 40$ and $Mt = 0.1$



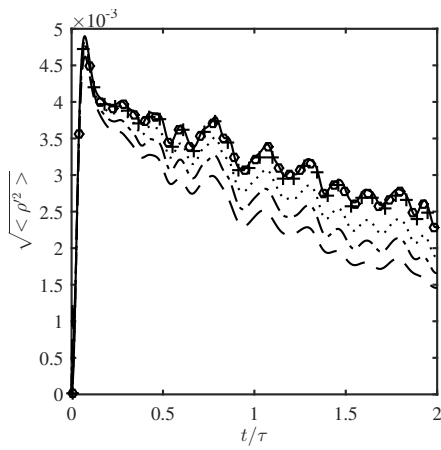
(b) TKE for $Re = 100$ and $Mt = 0.6$



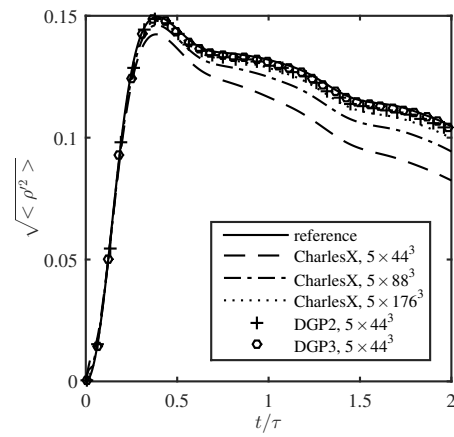
(c) Spectrum for $Re = 40$ and $Mt = 0.1$



(d) Spectrum for $Re = 100$ and $Mt = 0.6$



(e) Density RMS for $Re = 40$ and $Mt = 0.1$



(f) Density RMS for $Re = 100$ and $Mt = 0.6$

Figure 5. Turbulence quantities on tetrahedron meshes by both the DG and FV solvers.

The comparison is also conducted on a set of tetrahedral meshes. Due to the cell skewness and accuracy deterioration, CharlesX fails to compete with the DG scheme in terms of predictive accuracy. The predicted characteristic quantities are not comparable to those obtained by the DG scheme, even after two levels of mesh refinements (a factor of 64 in DoFs). The comparison underlines the benefit of DG in performing DNS/LES on complex geometries, and requires further demonstration.

Within the DG framework, the comparison between different polynomial orders is also conducted, for which DGP2 to DGP4 are considered and used with the same DoFs. It was found that higher-order polynomial approximation is superior in representing the density fluctuation characteristics at lower Mach-number turbulence. However, for highly compressible turbulence, the observation is reversed. Therefore, it is suggested the solution representation of different orders be adapted in accordance with the turbulent flow conditions. In general, higher-order approximations help resolving small scales, as found by examining the velocity spectra.

Acknowledgments

The authors would like to thank Dr. Jeonglae Kim, Hao Wu, and Qing Wang for helpful discussions.

REFERENCES

- ARNOLD, D. N., BREZZI, F., COCKBURN, B. & MARINI, L. D. 2002 Unified analysis of discontinuous Galerkin methods for elliptic problems. *SIAM J. Numer. Anal.* **39** (5), 1749–1779.
- BASSI, F. & REBAY, S. 1997 A high-order accurate discontinuous finite element method for the numerical solution of the compressible Navier–Stokes equations. *J. Comput. Phys.* **131** (2), 267–279.
- BASSI, F. & REBAY, S. 2000 GMRES discontinuous Galerkin solution of the compressible Navier–Stokes equations. In *Discontinuous Galerkin Methods: Theory, Computation and Applications* (ed. B. Cockburn & C.-W. Shu), pp. 197–208. Berlin: Springer.
- BECK, A. D., BOLEMANN, T., FLAD, D., FRANK, H., GASSNER, G. J., HINDENLANG, F. & MUNZ, C.-D. 2014 High-order discontinuous Galerkin spectral element methods for transitional and turbulent flow simulations. *Int. J. Numer. Meth. Fluids* **76** (8), 522–548.
- BODART, J., LARSSON, J. & MOIN, P. 2013 Large eddy simulation of high-lift devices. *AIAA Paper* 2013-2724.
- COCKBURN, B. & SHU, C.-W. 1998 The local discontinuous Galerkin method for time-dependent convection-diffusion systems. *SIAM J. Numer. Anal.* **35** (6), 2440–2463.
- DISKIN, B., THOMAS, J. L., NIELSEN, E. J., NISHIKAWA, H. & WHITE, J. A. 2010 Comparison of node-centered and cell-centered unstructured finite-volume discretizations: viscous fluxes. *AIAA J.* **48** (7), 1326–1338.
- FUREBY, C., TABOR, G., WELLER, H. G. & GOSMAN, A. D. 1997 A comparative study of subgrid scale models in homogeneous isotropic turbulence. *Phys. Fluids* **9** (5), 1416–1429.
- GASSNER, G. J. & BECK, A. D. 2013 On the accuracy of high-order discretizations for underresolved turbulence simulations. *Theor. Comp. Fluid. Mech.* **27** (3-4), 221–237.

- HAM, F. & IACCARINO, G. 2004 Energy conservation in collocated discretization schemes on unstructured meshes. *Annual Research Briefs*, Center for Turbulence Research, Stanford University, pp. 3–14.
- HICKEY, J.-P., MA, P. C., IHME, M. & THAKUR, S. S. 2013 Large eddy simulation of shear coaxial rocket injector: real fluid effects. *AIAA Paper* 2013-4071.
- KHALIGHI, Y., NICHOLS, J. W., LELE, S., HAM, F. & MOIN, P. 2011 Unstructured large eddy simulation for prediction of noise issued from turbulent jets in various configurations. *AIAA Paper* 2011-2886.
- KOSOVIĆ, B., PULLIN, D. I. & SAMTANEY, R. 2002 Subgrid-scale modeling for large-eddy simulations of compressible turbulence. *Phys. Fluids* **14** (4), 1511–1522.
- LARSSON, J., LAURENCE, S., BERMEJO-MORENO, I., BODART, J., KARL, S. & VICQUELIN, R. 2015 Incipient thermal choking and stable shock-train formation in the heat-release region of a scramjet combustor. part II: Large eddy simulations. *Combust. Flame* **162** (4), 907–920.
- LARSSON, J., LELE, S. K. & MOIN, P. 2007 Effect of numerical dissipation on the predicted spectra for compressible turbulence. *Annual Research Briefs*, Center for Turbulence Research, Stanford University, pp. 45–57.
- LV, Y. & IHME, M. 2015 Entropy-bounded discontinuous Galerkin scheme for Euler equations. *J. Comput. Phys.* **295**, 715–739.
- MOIN, P., SQUIRES, K., CABOT, W. & LEE, S. 1991 A dynamic subgrid-scale model for compressible turbulence and scalar transport. *Phys. Fluids* **3** (11), 2746–2757.
- NICHOLS, J. W., LELE, S. K., MOIN, P., HAM, F. E. & BRIDGES, J. E. 2012 Large-eddy simulation for supersonic rectangular jet noise prediction: effects of chevrons. *AIAA Paper* 2012-2212.
- PERAIRE, J. & PERSSON, P.-O. 2008 The compact discontinuous Galerkin (CDG) method for elliptic problems. *SIAM J. Sci. Comput.* **30** (4), 1806–1824.
- SHAHBAZI, K. 2005 An explicit expression for the penalty parameter of the interior penalty method. *J. Comput. Phys.* **205** (2), 401–407.
- TURKEL, E., RADESPIEL, R. & KROLL, N. 1997 Assessment of preconditioning methods for multidimensional aerodynamics. *Combust. Flame* **26** (6), 613–634.
- WANG, Z., FIDKOWSKI, K., ABGRALL, R., BASSI, F., CARAENI, D., CARY, A., DECONINCK, H., HARTMANN, R., HILLEWAERT, K., HUYNH, H., KROLL, N., MAY, G., PERSSON, P.-O., VAN LEER, B. & VISBAL, M. 2013 High-order CFD methods: current status and perspective. *Int. J. Numer. Meth. Fluids* **72**, 811–845.
- CARTON DE WIART, C., HILLEWAERT, K., BRICTEUX, L. & WINCKELMANS, G. 2015 Implicit LES of free and wall-bounded turbulent flows based on the discontinuous Galerkin/symmetric interior penalty method. *Int. J. Numer. Meth. Fluids* **78** (6), 335–354.
- CARTON DE WIART, C., HILLEWAERT, K., DUPONCHEEL, M. & WINCKELMANS, G. 2014 Assessment of a discontinuous Galerkin method for the simulation of vortical flows at high reynolds number. *Int. J. Numer. Meth. Fluids* **74** (7), 469–493.
- ZHANG, X. & SHU, C.-W. 2010 On positivity-preserving high order discontinuous Galerkin schemes for compressible Euler equations on rectangular meshes. *J. Comput. Phys.* **229** (23), 8918–8934.
- ZHANG, X. & SHU, C.-W. 2011 Positivity-preserving high order discontinuous Galerkin schemes for compressible Euler equations with source terms. *J. Comput. Phys.* **230** (4), 1238–1248.